crystals

MDPI

Article

Synthesis of a Novel Photocatalyst MVO_4/g-C_3N_4 (M = La, Gd) with Better Photocatalytic Activity for Tetracycline Hydrochloride Degradation under Visible-Light Irradiation

Zhengru Zhu, Songlin Han, Yongqiang Cao * and Junchao Jiang

School of Geography, Liaoning Normal University, Dalian 116029, China; zhengruzhu@lnnu.edu.cn (Z.Z.); mochawei475@163.com (S.H.); jiangjunchao@lnnu.edu.cn (J.J.)
* Correspondence: caoyongqiang@lnnu.edu.cn; Tel.: +86-0411-82159593

Abstract: In this study, novel photocatalysts MVO_4/g-C_3N_4 (M = La, Gd) were prepared by the hydrothermal method, through which different loading amounts of 10–50%MVO_4 and g-C_3N_4 were mixed and ultrasonically oscillated to gain heterojunction catalysts. All the samples were characterized by XRD, SEM, TEM, FT-IR, XPS, Us-vis, and PL to ensure the successful integration of $LaVO_4$ and $GdVO_4$ with g-C_3N_4. The obtained results showed that MVO_4/g-C_3N_4 could effectually improve the separation efficiency of photogenerated carriers during the photodegradation process, thus improving the photodegradation efficiency, while among them, 40%$GdVO_4$/g-C_3N_4 showed the best photocatalytic performance and degradation of tetracycline hydrochloride, reaching up to 91% for 3 h, which was 3.64 times higher than pristine g-C_3N_4. From the discussed results above, the possible mechanism of the photodegradation process was put forward. This study supplies a promising method to gain g-C_3N_4-based photocatalysts for antibiotics removal.

Keywords: heterojunction photocatalyst; vanadate; graphitic carbon nitride; antibiotic degradation

Citation: Zhu, Z.; Han, S.; Cao, Y.; Jiang, J. Synthesis of a Novel Photocatalyst MVO_4/g-C_3N_4 (M = La, Gd) with Better Photocatalytic Activity for Tetracycline Hydrochloride Degradation under Visible-Light Irradiation. *Crystals* **2021**, *11*, 756. https://doi.org/10.3390/cryst11070756

Academic Editor: Ferdinando Costantino and Eamor M. Woo

Received: 7 May 2021
Accepted: 25 June 2021
Published: 28 June 2021

1. Introduction

In recent years, antibiotic pollutants represented by tetracycline have been frequently detected in water, posing a great threat to the ecological environment and human health [1–4]. It is worth noting that compared with other antibiotics, tetracycline has the following features: biological accumulation and a long cycle [5]; natural attenuation with the passage of time, parts of the residual will not be degraded in environmental mediums but rather enter the body through the food chain [6]; it is a potential threat to the human body, the excessive intake may even affect human body physiology because it has severe carcinogenic, teratogenic and mutagenic consequences [7]. Therefore, finding a way to remove the tetracycline hydrochloride (TC) residues in the water environment is an urgent issue. At present, the methods used to remove tetracycline from wastewater and soil mainly include a physical method, chemical oxidation method [8], biodegradation method, etc. However, some traditional processing methods are limited in practical application due to their disadvantages, such as a complex process, high operating costs, and unstable effects. As of now, the application of advanced oxidation technology, especially semiconductor photocatalysis technology, in tetracycline wastewater treatment has been widely studied, and some research results have been achieved.

For a photocatalytic system with excellent performance, it is necessary to have a wide solar absorption range, high carrier separation and transmission efficiency, and strong redox capacity. Due to its simple synthesis method, unique electron band structure, and excellent photocatalytic cycling stability, g-C_3N_4 has become a hot research object of novel photocatalysts [9]. However, in actuality, the photocatalytic activity of g-C_3N_4 monomer materials is limited by the low utilization of sunlight and the high recombination rate of photogenerated electron holes [10,11]. Based on the semiconductor composite modification

of energy level matching, the interface heterojunction can be constructed by combining g-C_3N_4 with another semiconductor to improve the separation and transmission efficiency of photogenerated carriers, thus improving the photocatalytic efficiency [12].

In the present work, we prepared novel MVO_4/g-C_3N_4 (M = La, Gd) photocatalysts via the hydrothermal method. All the samples were further characterization by XRD, SEM, TEM, FT-IR, XPS, DRS, and PL. Moreover, TC was selected as a target pollutant and photodegradation experiments were performed under visible light irradiation. This study concentrated on the design of the novel heterojunction and its speculative mechanism of TC photodegradation under visible light.

2. Materials and Methods

2.1. Materials

Lanthanum nitrate hexahydrate, gadolinium nitrate hexahydrate, ammonium vanadate, melamine, ammonium hydroxide, sodium hydroxide, and tetracycline hydrochloride were purchased from China National Pharmaceutical Group Chemical Reagent Co. Ltd. (Shanghai, China). All the chemicals were analytic reagents.

2.2. Preparation of MVO_4/g-C_3N_4 (M = La, Gd) Nanocomposite

First, 15.0 g of melamine was placed into a covered crucible and heated to 550 °C, kept for 2 h, then cooled to room temperature. The obtained yellow powder was ground thoroughly for 10 min to get g-C_3N_4 nanosheets [13].

$LaVO_4$ and $GdVO_4$ were prepared via the hydrothermal method [14]. First, 0.52 g of sodium hydroxide and 1.52 g of NH_4VO_3 were added to 30 mL of deionized water and dissolved by stirring to obtain an aqueous solution of sodium metavanadate (A solution for short). Then, for $LaVO_4$, 5.84 g of lanthanum nitrate hexahydrate was added to a certain amount of water and dissolved by stirring to obtain B_1 solution. For $GdVO_4$, 5.62 g gadolinium nitrate hexahydrate was added into deionized water and stirred to obtain B_2 solution. The yellow suspension was formed by adding B_1 and B_2 solution to A solution slowly and respectively. After mixing and stirring for 30 min, the yellow suspension was added to the 200 mL Teflon-lined reaction autoclave and the temperature was kept at 200 °C for 48 h, then cooled naturally to room temperature. The milky white product was centrifuged and washed successively with water and anhydrous ethanol for three times. Finally, the obtained products were dried at 100 °C to form pure white $LaVO_4$ and $GdVO_4$ powder.

MVO_4/g-C_3N_4 composites were synthesized by ultrasonic dispersion method. A certain amount of pure g-C_3N_4 was added into 20 mL methanol, and the ultrasonic dispersion lasted for 30 min at room temperature. After 30 min, a certain amount of $LaVO_4$ and $GdVO_4$ powder were added, stirring the mixture for 2 h under the fume hood. Then, the resulting mixture was dried at 80 °C for 10 h. Finally, we placed the product in the crucible, in a muffle furnace, heating from 5 °C per minute to 250 °C and kept for 1 h, then naturally cooling to room temperature. The MVO_4/g-C_3N_4 composites were obtained. Lastly, 10%, 20%, 30%, 40%, and 50% MVO_4/g-C_3N_4 composite catalysts were prepared by adjusting the mass ratios of g-C_3N_4 and MVO_4 [15].

2.3. Characterization of Samples

For all the samples obtained, the X-ray powder diffraction patterns of the samples were measured on a Shimadzu LabX-6000 X-ray diffractometer equipped with Cu Kα radiation (λ = 0.15418 nm). A scanning electron microscope (SEM, Hitachi, S-4800, Tokyo, Japan) and transmission electron microscope (TEM, Hitachi, H-600, Japan) were utilized to characterize morphologies and nanostructures of the prepared samples. The functional groups and networks could be identified by the Fourier transform infrared (FT-IR, Bruker AXS, TENSOR-27, Karlsruhe, Germany) spectra, X-ray photoelectron spectroscopy (XPS, Thermo VG, ESCALAB-250, Waltham, MA, USA) measurements. The optical capacity was measured by UV-vis diffuse reflection spectroscopy (DRS, PerkinElmer, Lambda-35,

Waltham, MA, USA) and photoluminescence (PL, Shimadzu, RF-540, Kyoto, Japan) spectra. The total organic carbon (TOC) was measured on a TOC analyzer (Analytik Jena AG, MultiN/C2100TOC/TN, Jena, Germany).

2.4. Photodegradation Measurements

The photocatalytic activities of all the samples prepared were measured by the degradation of tetracycline in aqueous solution under visible light illumination. The light source was provided by a xenon lamp (CEAULIGHT, CEL-S500, Beijing, China) with a 420 nm cutoff filter. Then 20 mg of all the samples obtained was mixed with 100 mL of 20 mg/L tetracycline solution and magnetically stirred for 1 h to reach the adsorption–desorption equilibrium on the sample surface. Then, the xenon lamp was turned on, 5 mL of the suspension liquid was withdrawn and centrifuged and the absorbance the supernatant was measured by a UV–Vis spectrophotometer (MAPADA, UV-1800PC, Shanghai, China) at 356 nm.

3. Results and Discussion

3.1. Characterization Studies

The crystal phase structure of the catalyst prepared was analyzed using XRD, and the results are shown in Figure 1. As can be seen, the pure g-C_3N_4 (JCPDS 87-1526) [16] showed two diffraction peaks of (100) and (002) planes at 13.06° and 27.56°. The diffraction peaks of $GdVO_4$ were loaded at 18.67°, 24.66°, 33.28°, 35.2°, 37.7°, 40.08°, 44.64°, 47.74°, 49.16°, 50.5°, 57.1°, 61.9°, 64.1°, 69.78°, and 73.18°, which were matched to crystal plane (101), (200), (112), (220), (202), (301), (103), (321), (312), (400), (420), (332), (204), (224), and (512) of $GdVO_4$ (JCPDF No. 17-0260) [17]. $LaVO_4$ (JCPDS 50-0367) [18] was observed at 18.28°, 20.36°, 24.46°, 26.16°, 27.76°, 29.0°, 30.12°, 32.88°, 35.1°, 39.66°, 40.42°, 41.28°, 45.06°, 46.5°, 47.24°, 49.48°, 50.8°, 51.96°, 53.98°, 55.5°, 57.56°, 67.78°, 70.24°, and 73.32°, respectively, which corresponded to (011), (11-1), (020), (200), (120), (210), (012), (20-2), (21-2), (031), (31-1), (211), (212), (13-2), (103), (32-2), (132), (140), (40-2), (41-2), (21-4), (51-1), (41-4), and (33-4) planes. Nevertheless, the intensity of peaks at 20.26°, 27.76°, 30.12°, 35.1°, 45.06°, and 67.78° increased clearly with the amount of the $LaVO_4$ loading, indicating that more $LaVO_4$ particles were deposited on the surface of g-C_3N_4. In the XRD patterns of the MVO_4/g-C_3N_4 (M = La, Gd) composite catalysts, no impurity diffraction peaks were observed, which confirmed the successful synthesis of MVO_4/g-C_3N_4.

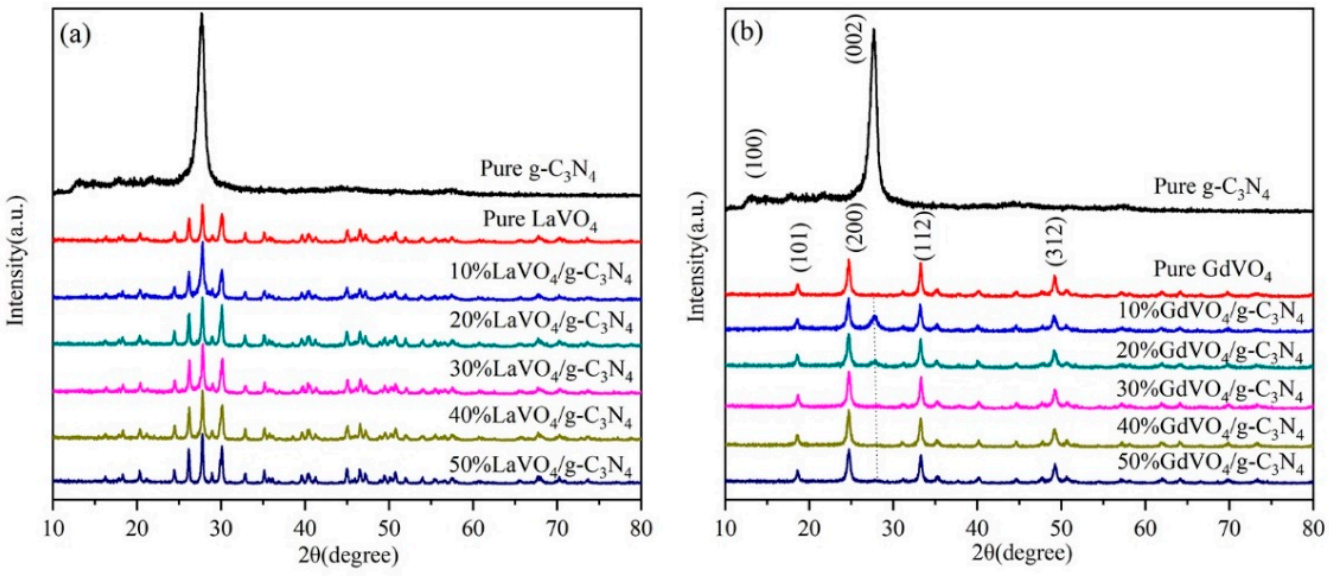

Figure 1. XRD patterns of (**a**) g-C_3N_4, $LaVO_4$, and 10–50%$LaVO_4$/g-C_3N_4, (**b**) g-C_3N_4, $GdVO_4$, and 10–50%$GdVO_4$/g-C_3N_4

To investigate the morphology and microstructure of the composite and its component parts. Scanning electron microscopy (SEM) and transmission electron microscopy (TEM) images are shown in Figure 2. As shown in Figure 2a, g-C_3N_4 exhibits nanosheet structure with a smooth surface. As seen in Figure 2b, pure $GdVO_4$ powders display a coral-like structure. It can be concluded from the TEM graph of $GdVO_4$/g-C_3N_4 (Figure 2c) that the composite catalyst has two parts, one with a black color and coral-like structure, belonging to the $GdVO_4$, and others with a French grey color and sheet-like structure of the g-C_3N_4. The morphology of pure $LaVO_4$ has a pin-like nanostructure, as shown in Figure 2d. In Figure 2e and the TEM graph of $LaVO_4$/g-C_3N_4 (Figure 2f), both $LaVO_4$ and g-C_3N_4 can be easily observed and $LaVO_4$ particles are well adhered to the surface of g-C_3N_4. Therefore, the constitution of MVO_4/g-C_3N_4 (M = La, Gd) composite is obviously recognizable, which is beneficial to the efficient transport of charge carriers in comparison to pure MVO_4 (M = La, Gd).

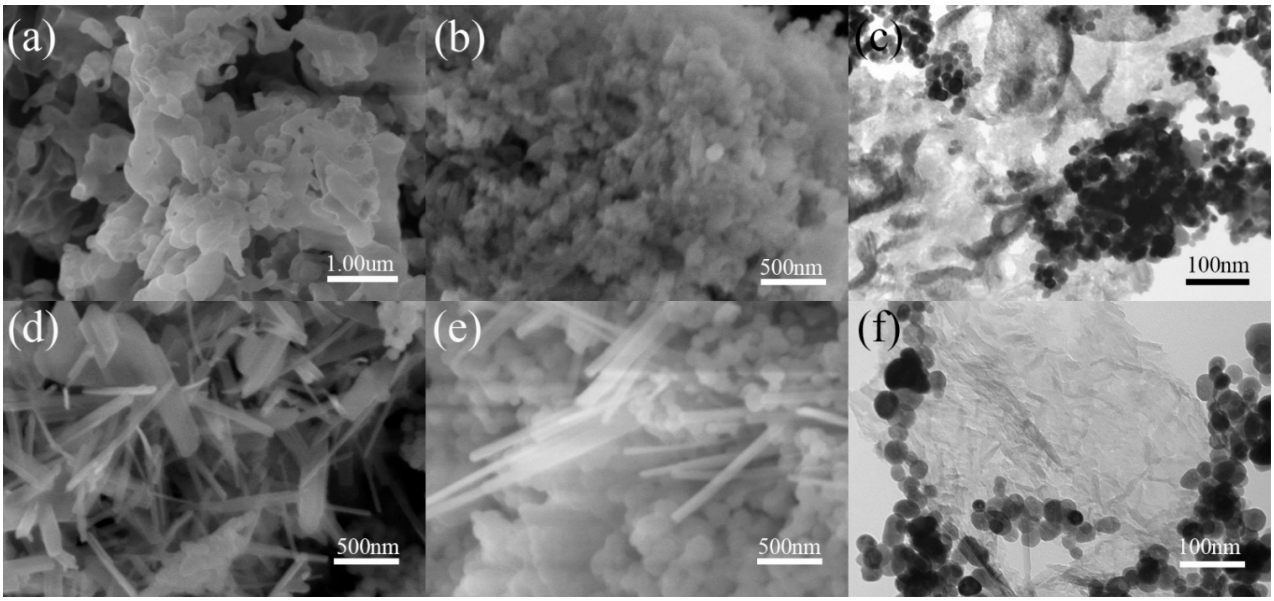

Figure 2. The SEM images of (**a**) g-C_3N_4, (**b**) $GdVO_4$, (**d**) $LaVO_4$, and (**e**) $LaVO_4$/g-C_3N_4 and the TEM images of (**c**) $GdVO_4$/g-C_3N_4 and (**f**) $LaVO_4$/g-C_3N_4.

FT-IR spectra of these synthesized samples are shown in Figure 3. In the case of MVO_4 (M = La, Gd), the two characteristic peaks at 810 and 440 cm^{-1} could be attributed to vibration of VO_4^{3-} [19], La-O [20] and Gd-O [21]. For pristine g-C_3N_4, the sharp peak at 1245, 1233, 1547, and 1633 cm^{-1} was vested in characteristic peak bands of C-N heterocyclic compounds. Apart from above peaks, the peak at 808 cm^{-1} is the characteristic absorption peak of the triazine ring. In addition, the multiple peaks at 3000–3700 cm^{-1} and 1100–1700 cm^{-1} are assigned to N-H stretching vibration and the C=N and C-N heterocyclic rings, respectively. Obviously, according to the results above, it was concluded that heterojunctions consist of MVO_4 (M = La, Gd) and g-C_3N_4.

In order to study surface chemical composition and oxidation state of all the obtained samples, XPS measurement was performed on MVO_4/g-C_3N_4 (M = La, Gd). As can be seen in Figure 4a, in which the XPS spectra of MVO_4/g-C_3N_4 (M = La, Gd) samples are displayed, these characteristic peaks of Gd, La, V, O, C, and N were observed expressly. In Figure 4b, the binding energy peaks at 168.3 eV, 144.9, and 139.3 eV are due to $Gd4d_{5/2}$ and $Gd4d_{3/2}$ [22]. In Figure 4c, the characteristic peaks at 853.6 and 849.4 eV are attributable to La $3d_{3/2}$, and the binding energy of 836.8 and 832.7 eV corresponds to La $3d_{5/2}$. As shown in the V 2p spectrum in Figure 4d, the binding energy peaks at 522.5 and 514.7 eV are ascribed to V $2p_{1/2}$ and V $2p_{3/2}$, and the V 2p peak is assigned to V^{5+} [23]. Moreover, the O 1s peaks at 529.8 eV and 527.9 eV in Figure 4e are in line with the O^{2-} and hydroxylated

oxygen atom adsorbed on the surface of MVO_4 (M = La, Gd), respectively. Then, the C 1s spectrum, as can be seen in Figure 4f, is fitted to two peaks at 285.2 eV and 281.8 eV, respectively, belonging to C-C coordination and sp^2 hybridized adventitious carbon atom in g-C_3N_4 or incompletely polymerized precursors [24]. For N 1s, Figure 4g shows three characteristic peaks of 401.5, 398.3, and 395.7 eV, which indicate that the nitrogen atom bonded to the surface hydrogen atom (N-H) and the tertiary nitrogen atom (N-$(C)_3$), and the nitrogen atom bonded to two carbon atom (C-N-C), respectively. Combining the XPS results above, we can conclude that MVO_4/g-C_3N_4 (M = La, Gd) composite were successfully synthesized.

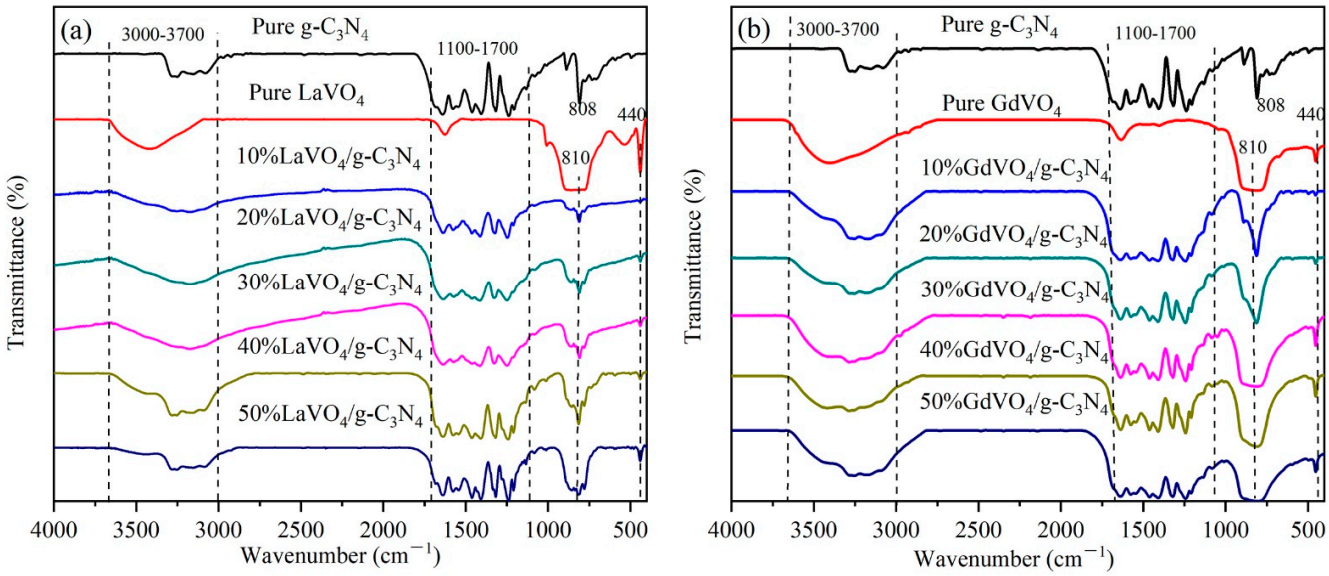

Figure 3. FT-IR absorbance spectra of (**a**) g-C_3N_4, $LaVO_4$, and 10–50%$LaVO_4$/g-C_3N_4, (**b**) g-C_3N_4, $GdVO_4$, and 10–50%$GdVO_4$/g-C_3N_4.

A comparison of UV-vis diffuse reflection spectra (DRS) of g-C_3N_4, $LaVO_4$, $GdVO_4$, and MVO_4/g-C_3N_4 (M = La, Gd) composite is shown in Figure 5a,b, and it is apparent that pure g-C_3N_4 displays efficient absorption at 460 nm. Compared with g-C_3N_4, MVO_4 (M = La, Gd) exhibits a wider band gap. As for MVO_4/g-C_3N_4 (M = La, Gd), it reveals stronger visible light absorption ability than pure g-C_3N_4. Overtly, with the amount of MVO_4 (M = La, Gd) increasing, absorption edges show a redshift, which contribute to formation of the heterojunction between MVO_4 (M = La, Gd) and g-C_3N_4, sequentially under the visible light range, and the absorption effective is significantly improved. In addition, the band gap value of all samples was estimated by Tauc formula.

As shown in Figure 5c–e, the bandgap energies of pure g-C_3N_4, pure $LaVO_4$, and pure $GdVO_4$ are 2.86, 3.47, and 3.54 eV, respectively, which are in keeping with the previous reports [25,26]. Moreover, the bandgap value of 20% $LaVO_4$/g-C_3N_4 was calculated to be 2.94 eV, severally. The bandgap value for 40% $GdVO_4$/g-C_3N_4 was 3.50 eV. Previous reports have suggested that lower band gap can promote the excitation and transition of electrons [27,28], thus improving the photocatalytic performance of the obtained materials.

Photoluminescence (PL) is another indicator of recombination of photogenerated electrons and holes [29], where low PL intensity suggests high separation of electron–hole pairs. The PL spectra of pristine g-C_3N_4, $LaVO_4$, $GdVO_4$, and different loadings of MVO_4/g-C_3N_4 (M = La, Gd) composite are displayed in Figure 6. Pure g-C_3N_4 has the highest PL spectral intensity, indicating that it is not an excellent photocatalyst because the carrier has the highest recombination intensity. The lowest PL intensity was observed for 40% $GdVO_4$/g-C_3N_4, which proves that this is probably the best photocatalyst studied in this study. Therefore, the observed quenching of luminescence intensity leads us to predict that MVO4/g-C3N4 (M = La, Gd) has

higher photocatalytic activity. Therefore, so far, the above analyses confirm that both MVO_4 (M = La, Gd) and g-C_3N_4 coexist in the composite photocatalysts.

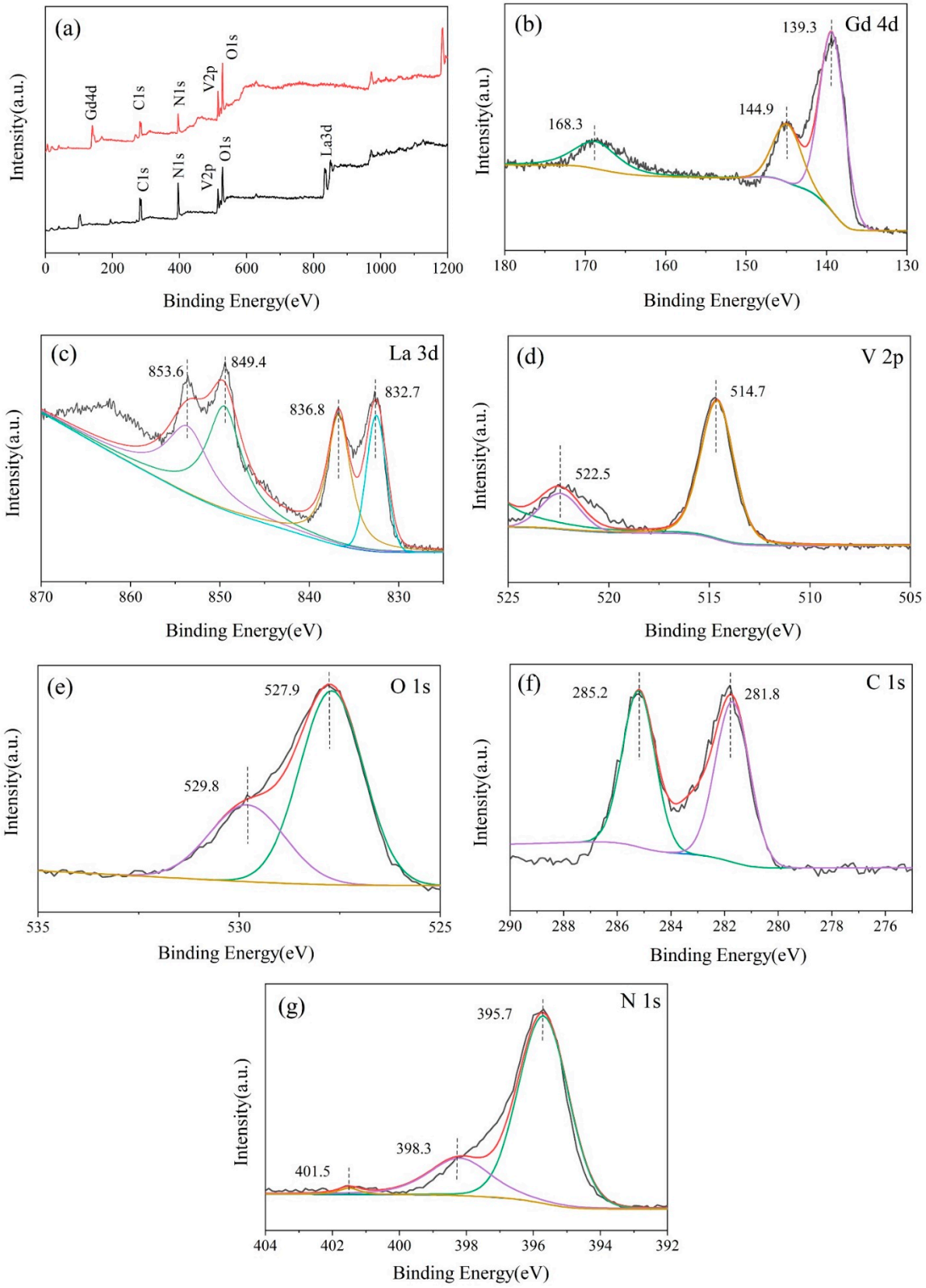

Figure 4. (**a**) XPS spectra of MVO_4/g-C_3N_4 (M = La, Gd) nanocomposites in a survey of the samples, (**b**) Gd 4d, (**c**) La 3d, (**d**) V 2p, (**e**) O 1s, (**f**) C 1s, and (**g**) N 1s.

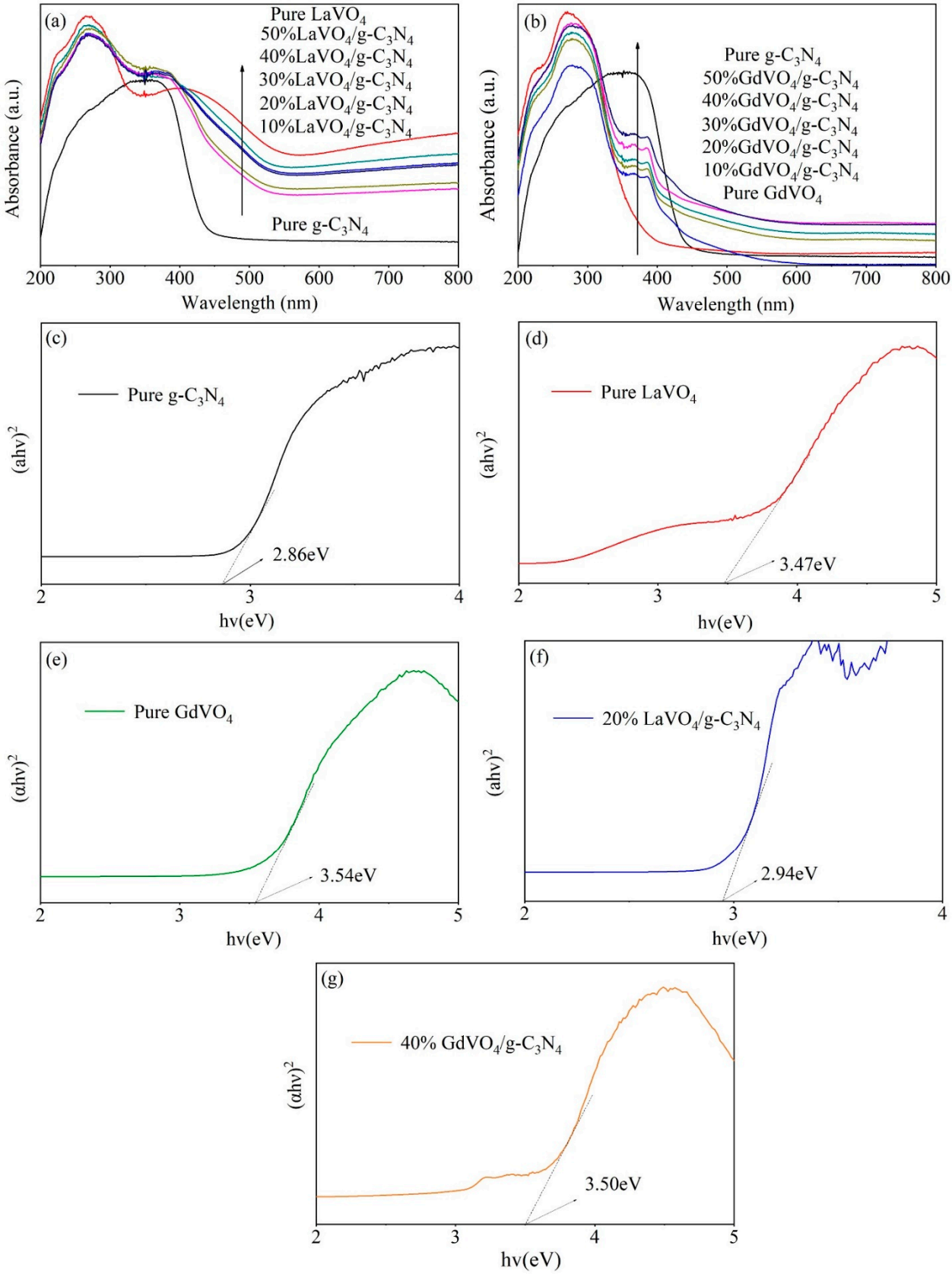

Figure 5. DRS spectra of (**a**)10–50% $LaVO_4$/g-C_3N_4, (**b**) 10–50%$GdVO_4$/g-C_3N_4, and the band gaps of (**c**) g-C_3N_4, (**d**) $LaVO_4$, (**e**) $GdVO_4$, (**f**) 20% $LaVO_4$/g-C_3N_4, and (**g**) 40% $GdVO_4$/g-C_3N_4.

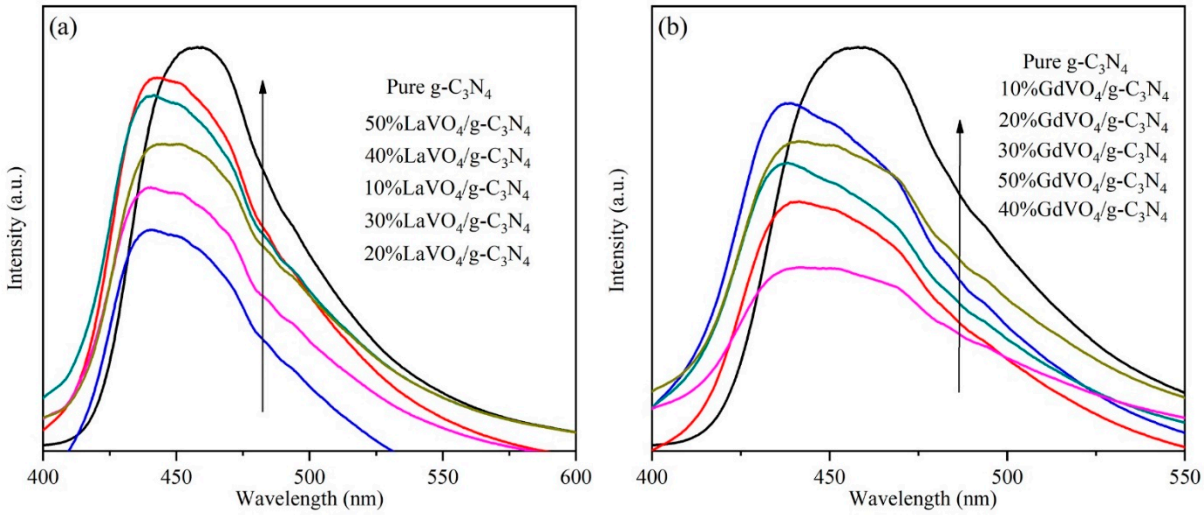

Figure 6. The photoluminescence of (**a**) g-C_3N_4 and 10–50%$LaVO_4$/g-C_3N_4, (**b**) g-C_3N_4 and 10–50%$GdVO_4$/g-C_3N_4.

3.2. Photocatalytic Performance

The photocatalytic performance of the obtained samples was evaluated by photooxidation degradation of TC under visible light. As displayed in Figure 7a, for the g-C_3N_4, $LaVO_4$, and $GdVO_4$, the photocatalytic degradation efficiencies of TC are just 25.3%, 32.8%, and 51.0% under visible light for 3 h, respectively. Based on the loading amount of $LaVO_4$, from 10% to 50%, the degradation efficiencies of TC, improved, reaching to 63.2%, 79.1%, 69.8%, 53.6%, and 52.4%. As for a 10–50% loading amount of $GdVO_4$ the degradation efficiencies of TC reached to 68.0%, 73.4%, 82.4%, 91%, and 84.9% respectively. It can be easily observed that 40% $GdVO_4$/g-C_3N_4 has the best photodegradation efficiency among these obtained samples. The reasons why the $GdVO_4$/g-C_3N_4 composite can enhance photocatalytic activities are assigned to the following: (1) with the increase of $GdVO_4$, the $GdVO_4$/g-C_3N_4 heterojunctions could obtain more visible light, which leads to red shift of absorption edges; (2) the $GdVO_4$/g-C_3N_4 heterojunctions would efficiently restrain recombination of photogenerated charge pairs. In addition, the Langmuir–Hinshelwood model formula is as follows, which was used to fit reaction kinetics:

$$\ln(C_0/C_t) = kt \quad (1)$$

where C_0, C_t, and t represent the original concentration, final concentration, and reaction time, respectively, and k is the kinetic constant. Combining Figure 7b and Table 1, it can be concluded that the kinetic constants of TC photodegradation over 40% $LaVO_4$/g-C_3N_4 (0.01302 min^{-1}) is 7.44 times that of pristine g-C_3N_4 (0.00175 min^{-1}), indicating that the coupling g-C_3N_4 with $GdVO_4$ extremely enhances photodegradation efficiency of TC among these photocatalysts.

Moreover, the changes in the TOC reflected the degree of mineralization of an organic molecule during testing period. To further prove the photocatalytic degradation effect, we measured the degree of mineralization before and after the degradation of the target pollutants. The results showed that if there was no impurity in the TC solution, the TOC concentration was 21.09 mg/L, and after degradation with 40% $GdVO_4$/g-C_3N_4 as photocatalysts, the residual TOC was about 4.37 mg/L. Apparently, the TOC results indicated that the 40% $GdVO_4$/g-C_3N_4 could not only degrade TC but also mineralize it under visible light irradiation, working as an efficient photocatalyst to degrade TC in wastewater.

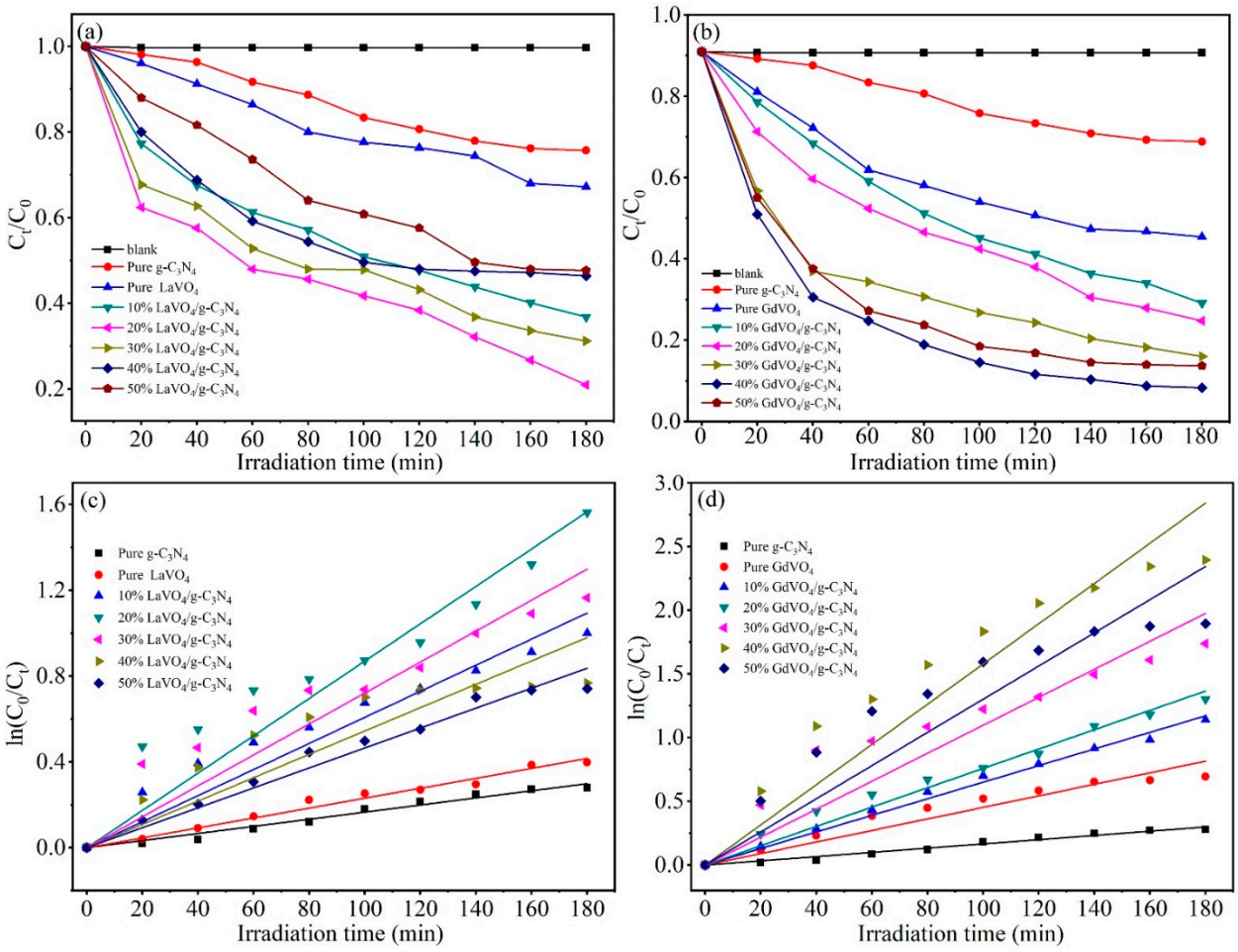

Figure 7. Photocatalytic performance of (**a**) g-C_3N_4, $LaVO_4$, and 10–50%$LaVO_4$/g-C_3N_4, (**b**) g-C_3N_4, $GdVO_4$, and 10–50%$GdVO_4$/g-$C_3N_4$and kinetic curves of (**c**) g-C_3N_4, $LaVO_4$, and 10–50%$LaVO_4$/g-C_3N_4, (**d**) g-C_3N_4, $GdVO_4$, and 10–50%$GdVO_4$/g-C_3N_4.

Table 1. Photocatalytic results of all samples.

Sample Name	Degradation (%)	K (min^{-1})	R^2
g-C_3N_4	25.3%	0.00 166	0.99 093
$LaVO_4$	32.8%	0.00 225	0.97 831
$GdVO_4$	51.0%	0.00 453	0.97 748
10% $LaVO_4$/g-C_3N_4	63.2%	0.00 503	0.96 199
20% $LaVO_4$/g-C_3N_4	79.1%	0.00 717	0.94 071
30% $LaVO_4$/g-C_3N_4	69.8%	0.00 565	0.93 048
40% $LaVO_4$/g-C_3N_4	53.6%	0.00 399	0.82 037
50% $LaVO_4$/g-C_3N_4	52.4%	0.00 430	0.97 268
10% $GdVO_4$/g-C_3N_4	68.0%	0.00 651	0.99 711
20% $GdVO_4$/g-C_3N_4	73.4%	0.00 759	0.99 278
30% $GdVO_4$/g-C_3N_4	82.4%	0.01 097	0.95 985
40% $GdVO_4$/g-C_3N_4	91.0%	0.01 578	0.96 861
50% $GdVO_4$/g-C_3N_4	84.9%	0.01 302	0.95 533

3.3. Photodegradation Mechanism

We further explored the possible mechanism of $GdVO_4$/g-C_3N_4 photodegradation of TC, which was shown in Figure 8. According to the DRS analysis of all the samples, the edge of the corresponding band energies (E_g) of pure g-C_3N_4 and pristine $GdVO_4$ were

approximately 2.86 eV and 3.54 eV. The valence band (VB) and conduction band (CB) of samples were calculated by following formula:

$$E_{VB} = X - E_e + 0.5\,E_g \quad (2)$$

$$E_{CB} = E_{VB} - E_g \quad (3)$$

where X is the absolute electronegativity of semiconductors [30], E_e is the energy of free electrons compared to hydrogen (4.5 eV), and E_g is the bandgap of materials. It was calculated that the E_{CB} and E_{VB} of g-C_3N_4 were −1.11 eV and 1.75 eV, and of $GdVO_4$ were −0.34 eV and 3.20 eV. The semiconductor coupling effect between $GdVO_4$ and g-C_3N_4 induces electron migration from the g-C_3N_4 conduction band to the $GdVO_4$ conduction band, and hole migration from the $GdVO_4$ valence band to g-C_3N_4 valence band. Specifically, the photoexcited electrons on the CB of g-C_3N_4 can react with O_2 to generate the $\cdot O_2^-$ because their CB potential values were lower than $O_2/\cdot O_2^-$ potential values (−0.33 eV vs. NHE), while the holes on the VB of $LaVO_4$ can react with H_2O and OH^- to form ·OH on account of the fact that the VB potential of $GdVO_4$ was higher than $\cdot OH/OH^-$ potential (1.99 eV vs. NHE) [18]. Then, $\cdot O_2^-$ and ·OH participated in the degradation of TC. Furthermore, the possible degradation process is displayed in the following equations:

$$GdVO_4/g\text{-}C_3N_4 + h\nu \rightarrow GdVO_4/g\text{-}C_3N_4\ (e^-_{CB} + h^+_{VB}) \quad (4)$$

$$h^+ + OH^- \rightarrow \cdot OH \quad (5)$$

$$h^+ + H_2O \rightarrow \cdot OH + H^+ \quad (6)$$

$$e^- + O_2 \rightarrow \cdot O_2^- \quad (7)$$

$$TC + \cdot O_2^-/\cdot OH \rightarrow H_2O + CO_2 \quad (8)$$

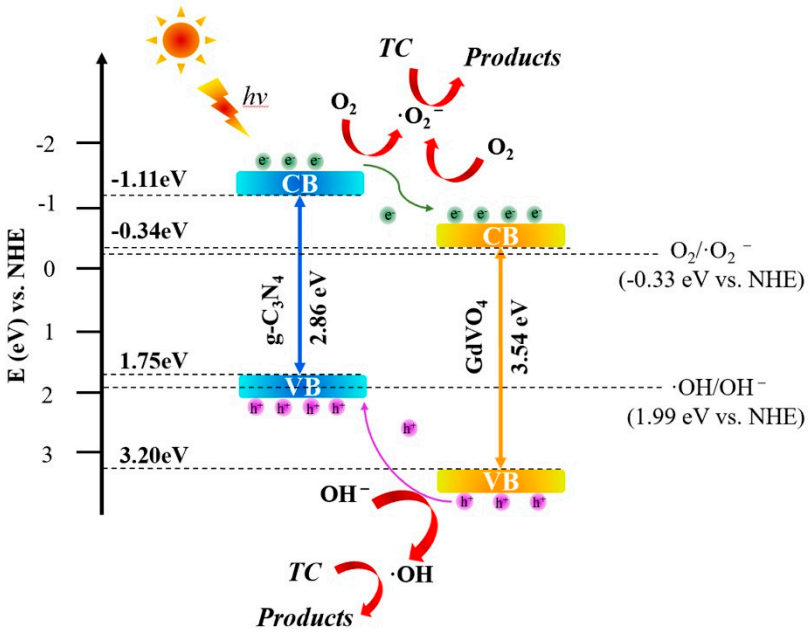

Figure 8. The possible degradation mechanism of $GdVO_4/g\text{-}C_3N_4$ composite.

4. Conclusions

In conclusion, a novel $MVO_4/g\text{-}C_3N_4$ (M = La, Gd) nanocomposite material was prepared by a facile hydrothermal method. This novel photocatalyst has the activity of initiating the decomposition of TC under visible light illuminate. As shown in XRD and FT-IR results, there were no impurity diffraction peaks observed, which confirmed

the successful synthesis of MVO_4/g-C_3N_4. We also observed that, in the SEM and TEM results, both the pin-like $LaVO_4$ and coral-like $GdVO_4$ were successful in loading on the sheet g-C_3N_4, respectively. And the results of DRS and PL characterization showed that MVO has more efficient visible light response ability. In addition, it also exhibits excellent photocatalytic performance under ultraviolet light irradiation. The enhanced photocatalytic performance of $GdVO_4$/g-C_3N_4 is not only related to the energy band potential of $GdVO_4$ and g-C_3N_4, but also related to the interconnected nanocrystalline heterojunction of g-C_3N_4. This study may provide an important strategy for the designation and preparation of high-performance photocatalysts induced by visible light.

Author Contributions: Supervision, J.J.; Visualization, Y.C.; Writing—original draft, S.H.; Writing – review & editing, Z.Z. All authors have read and agreed to the published version of the manuscript.

Funding: This research was funded by "Coupling mechanism and simulation of water, energy and grain for efficient utilization of water resources in northeast agricultural region", grant number 52079060 and The APC was funded by National Natural Science Foundation of China.

Institutional Review Board Statement: Not applicable.

Informed Consent Statement: Page: 11 Informed consent was obtained from all subjects involved in the study.

Data Availability Statement: Not applicable.

Conflicts of Interest: The authors declare no conflict of interest.

References

1. Jallouli, N.; Pastrana-Martínez, L.M.; Ribeiro, A.R.; Moreira, N.F.F.; Faria, J.L.; Hentati, O.; Silva, A.M.T.; Ksibi, M. Heterogeneous photocatalytic degradation of ibuprofen in ultrapure water, municipal and pharmaceutical industry wastewaters using a TiO_2/UV-LED system. *Chem. Eng. J.* **2018**, *334*, 976–984. [CrossRef]
2. Caban, M.; Lis, E.; Kumirska, J.; Stepnowski, P. Determination of pharmaceutical residues in drinking water in Poland using a new SPE-GC-MS(SIM) method based on Speedisk extraction disks and DIMETRIS derivatization. *Sci. Total Environ.* **2015**, *538*, 402–411. [CrossRef] [PubMed]
3. Sim, W.J.; Kim, H.Y.; Choi, S.D.; Kwon, J.H.; Oh, J.E. Evaluation of pharmaceuticals and personal care products with emphasis on anthelmintics in human sanitary waste, sewage, hospital wastewater, livestock wastewater and receiving water. *J. Hazard. Mater.* **2013**, *248–249*, 219–227. [CrossRef]
4. Wang, K.; Zhang, G.; Li, J.; Li, Y.; Wu, X. 0D/2D Z-Scheme heterojunctions of bismuth tantalate quantum Dots/Ultrathin g-C_3N_4 nanosheets for highly efficient visible light photocatalytic degradation of antibiotics. *ACS Appl. Mater. Interfaces* **2017**, *9*, 43704–43715. [CrossRef] [PubMed]
5. Halling-Sørensen, B.; Sengeløv, G.; Tjørnelund, J. Toxicity of tetracyclines and tetracycline degradation products to environmentally relevant bacteria, including selected tetracycline-resistant bacteria. *Arch. Environ. Contam. Toxicol.* **2002**, *42*, 263–271. [CrossRef] [PubMed]
6. López-Peñalver, J.J.; Sánchez-Polo, M.; Gómez-Pacheco, C.V.; Rivera-Utrilla, J. Photodegradation of tetracyclines in aqueous solution by using UV and UV/H_2O_2 oxidation processes. *J. Chem. Technol. Biotechnol.* **2010**, *85*, 1325–1333. [CrossRef]
7. Golub, L.M.; Lee, H.M.; Ryan, M.E.; Giannobile, W.V.; Payne, J.; Sorsa, T. Tetracyclines inhibit connective tissue breakdown by multiple non-antimicrobial mechanisms. *Adv. Dent. Res.* **1998**, *12*, 12–26. [CrossRef]
8. Piumetti, M.; Fino, D.; Russo, N. Mesoporous manganese oxides prepared by solution combustion synthesis as catalysts for the total oxidation of VOCs. *Appl. Catal. B Environ.* **2015**, *163*, 277–287. [CrossRef]
9. Wang, Y.; Wang, X.; Antonietti, M. Polymeric graphitic carbon nitride as a heterogeneous organocatalyst: From photochemistry to multipurpose catalysis to sustainable chemistry. *Angew. Chemie Int. Ed.* **2012**, *51*, 68–89. [CrossRef]
10. Masih, D.; Ma, Y.; Rohani, S. Graphitic C_3N_4 based noble-metal-free photocatalyst systems: A review. *Appl. Catal. B Environ.* **2017**, *206*, 556–588. [CrossRef]
11. Mohini, R.; Lakshminarasimhan, N. Coupled semiconductor nanocomposite g-C_3N_4/TiO_2 with enhanced visible light photocatalytic activity. *Mater. Res. Bull.* **2016**, *76*, 370–375. [CrossRef]
12. Wen, J.; Xie, J.; Chen, X.; Li, X. A review on g-C_3N_4-based photocatalysts. *Appl. Surf. Sci.* **2017**, *391*, 72–123. [CrossRef]
13. Che, H.; Ngaw, C.K.; Hu, P.; Wang, J.; Li, Y.; Wang, X.; Teng, W. Fabrication of molybdenum doped carbon nitride nanosheets for efficiently photocatalytic water splitting. *J. Alloys Compd.* **2020**, *849*, 156440. [CrossRef]
14. Veldurthi, N.K.; Eswar, N.K.R.; Singh, S.A.; Madras, G. Cocatalyst free Z-schematic enhanced H_2 evolution over $LaVO_4$/$BiVO_4$ composite photocatalyst using Ag as an electron mediator. *Appl. Catal. B Environ.* **2018**, *220*, 512–523. [CrossRef]
15. Huang, H.; Li, D.; Lin, Q.; Zhang, W.; Shao, Y.; Chen, Y.; Sun, M.; Fu, X. Efficient degradation of benzene over $LaVO_4$/TiO_2 nanocrystalline heterojunction photocatalyst under visible light irradiation. *Environ. Sci. Technol.* **2009**, *43*, 4164–4168. [CrossRef]

16. Wang, N.; Li, J.; Wu, L.; Li, X.; Shu, J. MnO_2 and carbon nanotube co-modified C_3N_4 composite catalyst for enhanced water splitting activity under visible light irradiation. *Int. J. Hydrogen Energy* **2016**, *41*, 22743–22750. [CrossRef]
17. Thirumalai, K.; Shanthi, M.; Swaminathan, M. Natural sunlight active $GdVO_4$-ZnO nanomaterials for photo-electrocatalytic and self-cleaning applications. *J. Water Process Eng.* **2017**, *17*, 149–160. [CrossRef]
18. Xu, Y.; Liu, J.; Xie, M.; Jing, L.; Xu, H.; She, X.; Li, H.; Xie, J. Construction of novel CNT/$LaVO_4$ nanostructures for efficient antibiotic photodegradation. *Chem. Eng. J.* **2019**, *357*, 487–497. [CrossRef]
19. Silversmit, G.; Depla, D.; Poelman, H.; Marin, G.B.; De Gryse, R. Determination of the V2p XPS binding energies for different vanadium oxidation states (V^{5+} to V^{0+}). *J. Electron Spectros. Relat. Phenom.* **2004**, *135*, 167–175. [CrossRef]
20. Sivakumar, V.; Suresh, R.; Giribabu, K.; Narayanan, V. Characterization and visible light driven photocatalytic activity of (M = Bi, La)MVO_4@poly(o-phenylenediamine) nanocomposite. *Mater. Sci. Eng. B Solid-State Mater. Adv. Technol.* **2019**, *240*, 41–48. [CrossRef]
21. Thakur, H.; Singh, B.P.; Kumar, R.; Gathania, A.K.; Singh, S.K.; Singh, R.K. Synthesis, structural analysis, upconversion luminescence and magnetic properties of Ho^{3+}/Yb^{3+} co-doped $GdVO_4$ nanophosphor. *Mater. Chem. Phys.* **2020**, *253*, 123333. [CrossRef]
22. Jaganathan, S.K.; John Peter, A.; Venkatakrishnan, M.; Krishnan, R. Hydrothermal synthesis, characterization and luminescence properties of $CaGd_2(MoO_4)_4$:Eu^{3+} ovoid like structures. *New J. Chem.* **2017**, *41*, 14977–14986. [CrossRef]
23. Vairapperumal, T.; Natarajan, D.; Manikantan Syamala, K.; Kalarical Janardhanan, S.; Balachandran Unni, N. Catechin caged lanthanum orthovanadate nanorods for nuclear targeting and bioimaging applications. *Sens. Actuators B Chem.* **2017**, *242*, 700–709. [CrossRef]
24. Zhang, F.; Tang, J.; Wang, Z.; Qin, L.C. Graphene-carbon nanotube composite aerogel for selective detection of uric acid. *Chem. Phys. Lett.* **2013**, *590*, 121–125. [CrossRef]
25. Chu, S.; Wang, Y.; Guo, Y.; Feng, J.; Wang, C.; Luo, W.; Fan, X.; Zou, Z. Band structure engineering of carbon nitride: In search of a polymer photocatalyst with high photooxidation property. *ACS Catal.* **2013**, *3*, 912–919. [CrossRef]
26. Shandilya, P.; Mittal, D.; Sudhaik, A.; Soni, M.; Raizada, P.; Saini, A.K.; Singh, P. $GdVO_4$ modified fluorine doped graphene nanosheets as dispersed photocatalyst for mitigation of phenolic compounds in aqueous environment and bacterial disinfection. *Sep. Purif. Technol.* **2019**, *210*, 804–816. [CrossRef]
27. Jiang, L.; Yuan, X.; Zeng, G.; Chen, X.; Wu, Z.; Liang, J.; Zhang, J.; Wang, H.; Wang, H. Phosphorus- and sulfur-codoped g-C_3N_4: facile preparation, mechanism insight, and application as efficient photocatalyst for tetracycline and methyl orange degradation under visible light irradiation. *ACS Sustain. Chem. Eng.* **2017**, *5*, 5831–5841. [CrossRef]
28. Khataee, A.; Soltani, R.D.C.; Karimi, A.; Joo, S.W. Sonocatalytic degradation of a textile dye over Gd-doped ZnO nanoparticles synthesized through sonochemical process. *Ultrason. Sonochem.* **2015**, *23*, 219–230. [CrossRef]
29. Chang, W.S.; Li, Y.C.M.; Chung, T.W.; Lin, Y.S.; Huang, C.M. Toluene decomposition using silver vanadate/SBA-15 photocatalysts: DRIFTS study of surface chemistry and recyclability. *Appl. Catal. A Gen.* **2011**, *407*, 224–230. [CrossRef]
30. Zhang, J.; Zhu, Z.; Jiang, J.; Li, H. Ultrasound-Assisted hydrothermal fabrication of AgI/$MFeO_3$/g-C_3N_4 (M = Y, Gd, La) nano sheet-sphere-sheet photocatalysts with enhanced photodegradation activities for norfloxacin. *Catalysts* **2020**, *4*, 373. [CrossRef]